RSC Advances

ROYAL SOCIETY OF CHEMISTRY

PAPER

View Article Online
View Journal | View Issue

Cite this: *RSC Adv.*, 2025, **15**, 13940

Combining nanotechnology and nanohybrid methods to improve the physical and chemical properties of CuS and boost its photocatalytic aptitude

Javaria Naseem,[a] Mohamed. Abdel Rafea,[b] Magdi E. A. Zaki,[c] Mohamed Ibrahim Attia,[c] Mohamed. R. El-Aassar,[d] Faisal Alresheedi,[e] Sonia Zulfiqar[f] and Muhammad Aadil *[a]

Received 25th January 2025
Accepted 18th April 2025

DOI: 10.1039/d5ra00602c

rsc.li/rsc-advances

This study used a simple chemical method followed by ultrasonication to make copper sulfide (CuS) nanoparticles and their carbon nanotube-based nanohybrid (CuS–CNTs). To characterize the catalysts, different methods were employed. XRD was used to confirm that the CNTs were integrated with the crystalline structure, FTIR was used to detect functional groups, and SEM-EDX further verified the catalysts' shape and make-up. The addition of CNTs enhanced the optical, optoelectronic, and electrical properties of CuS by preventing particle adhesion. UV-Vis, photoluminescence, and current–voltage tests showed that the material could absorb more light, stop charges from combining, and move charges more efficiently. Carbon content, moisture absorption, and thermal stability were evaluated through TGA analysis. The nanohybrid had great photocatalytic activity in visible light, breaking down all of the MB dye in 90 min. In comparison, bare CuS only mineralizes 65.9% of the dye in 100 min. The reaction rate constant (k) was calculated to be 0.024 min^{-1}. The nanohybrid's stability was shown by the fact that it lost only 2.15% of its efficiency over five cycles of reusability tests. Additionally, this study shows that nanotechnology and composite materials can improve semiconductor photocatalysis, which could be useful for cleaning up the environment.

1. Introduction

The remarkable surge in population growth necessitates the establishment of numerous industries, which are essential for meeting basic needs and integrating cutting-edge technology for convenience. These industries play a crucial role in ensuring human survival, but unfortunately, they release untreated waste effluents that contain organic acids, poisonous gases, toxins, bleaching agents, antibiotics, and organic dyes. These pollutants enter public water sources and pollute the water, causing harm to ecosystems, public health, and a shortage of clean water, a vital resource for all life.[1,2] The most threatening pollutants are toxic dyes, which are non-biodegradable and exhibit exceptional stability against heat, chemicals, and light due to their intricate aromatic structure. The primary source of organic dyes is untreated wastewater from the tanning, textile, pharmaceutical, paper processing, culinary, and plastic industries.[3] About 2 million tons of waste pollutants and 490 tons of dyes are indiscriminately dumped into waterways daily.[4,5] This terrifying prospect requires strict laws, sustainable industrial practices, and proper wastewater treatment to protect water sources.[6,7]

The most significant challenge is identifying the most effective method of effluent treatment that is affordable, environmentally friendly, and effective. Current methods, such as ion-exchange resins, adsorption, membrane filtration, precipitation-aggregation, electrolytic purification, ozonation, and biochemical techniques, have not always proven effective in addressing this issue.[8–10] This problem arises because these methods have limitations, such as creating secondary pollutants, not fully breaking down the dye, not being able to absorb much dye, and taking a long time. Furthermore, the high cost and energy consumption of these techniques exacerbate the substantial financial burden they impose on industries.[11] Photocatalysis using semiconductor photocatalysts, an attractive alternative to existing approaches, has received interest in

---

[a] *Department of Chemistry, The Islamia University of Bahawalpur, Pakistan. E-mail: aadilkhanmundhali@gmail.com; Muhammad.aadil@iub.edu.pk*

[b] *Imam Mohammad Ibn Saud Islamic University (IMSIU), College of Science, Department of Physics, Riyadh, 11623, Kingdom of Saudi Arabia*

[c] *Department of Chemistry, College of Science, Imam Mohammad Ibn Saud Islamic University (IMSIU), Riyadh, 11623, Kingdom of Saudi Arabia*

[d] *Department of Chemistry, College of Science, Jouf University, PO Box 2014, Sakaka, Aljouf, Saudi Arabia*

[e] *Department of Physics, College of Science, Qassim University, Buraidah 51452, Saudi Arabia*

[f] *Department of Physical Sciences, Lander University, 320 Stanley Ave, Greenwood, South Carolina 29649, USA*

response to this difficult challenge.[12,13] The dye is completely degraded, no secondary pollutants are produced, working conditions are gentle, and it employs the sunlight, a renewable energy source, making it eco-friendly and cost-effective.[14]

Photocatalytic degradation of pollutants is influenced by several key factors, including the initial pollutant concentration, solution pH, temperature, dissolved oxygen levels, and catalyst dose. All of these factors can be optimized. Therefore, selecting the ideal materials with the appropriate band structure, high surface properties, effective light absorption, and efficient charge separation is crucial for ensuring an efficient photocatalytic process.[15] Transitional oxides, in their capacity as semiconducting photocatalysts, encounter substantial obstacles. Initially, their bandgaps limit their light absorption to the ultraviolet (UV), which comprises only 5% of the total solar spectrum.[16] Secondly, the population of charge carriers is diminished by prompt charge recombination. Finally, the degradation reaction kinetics are impeded by the deficient charge transport properties. Copper sulfide (CuS), having a lower bandgap energy of 2.10 eV, can successfully consume visible light and use 50% of solar energy as a photocatalyst. It stands out for its superior optical and electrical qualities, nontoxicity, thermal and photochemical stability, and ease of recycling.[17–19] Its availability and endurance make it a very promising material for photocatalytic applications.

Researchers have used nanostructured formation, doping,[20] co-doping, composite creation, and heterojunction construction to improve CuS photocatalytic performance. The review of the literature suggests making nanostructured CuS and sticking highly conductive carbonaceous matrices to them to improve charge transfer and light collection, which improves photocatalysis work. Carbon nanotubes (CNTs) can significantly enhance the photocatalytic activity of semiconductor materials through various mechanisms. They act as electron sinks, capturing excited electrons; provide a large surface area to facilitate interactions between pollutants and the photocatalyst; enhance light absorption due to their carbonaceous nature; exhibit high conductivity, aiding in the transfer of photogenerated electrons to the catalyst's surface; and contribute to structural stability, extending the catalyst's lifespan.[21,22]

In the current work, we have synthesized bare copper sulfide nanoparticles (NPs) and their carbon nanotube (CNT)-supported nanohybrid *via* a facile chemical route. Unlike conventional CuS-based photocatalysts, the present study strategically integrates CuS nanoparticles with carbon nanotubes (CNTs) to engineer a composite with enhanced photocatalytic performance. The incorporation of CNTs not only broadens the light absorption range due to their carbonaceous nature but also significantly improves charge carrier dynamics by facilitating efficient electron transport and suppressing electron–hole recombination. This synergistic design addresses the intrinsic limitations of pure CuS systems and offers a dual-functionality approach where CNTs serve as both electron sinks and a conductive network. Consequently, this work provides a comprehensive strategy to enhance photocatalytic efficiency, offering a notable advancement over previously reported CuS-based photocatalysts.

2. Experimental

2.1 Chemicals

Copper acetate monohydrate [$Cu(CH_3COO)_2\cdot H_2O$]; 99%, thiourea [$(NH_2)_2CS$]; 99%, and potassium hydroxide (KOH); 90% were procured from Merck, while ethanol (C_2H_5OH); 99.5% and CNTs (95%) were supplied by Sigma-Aldrich for the fabrication of CuS-CNT nanohybrids.

2.2 Synthesis of copper sulfide (CuS)

Copper sulfide nanoparticles were synthesized using a facile wet-chemical technique. Copper(II) acetate monohydrate (15 mmol) was dissolved in deionized water with constant stirring to prepare 150 mL of a 0.1 M solution as a precursor salt solution. Thiourea (15 mmol) was dissolved in water to prepare 150 mL of a 0.1 M solution as a sulfur source and surfactant. The precursor salt solution was turned bluish-green on slowly adding thiourea solution and stirring at room temperature for 10 min. Since thiourea decomposition to generate S^{2-} is significant at high temperature and alkaline pH, the temperature of the precursor salt solution was maintained at 60–70 °C and the pH at 9–10, with continuous stirring for 45 min. A dilute NaOH solution was used to keep the reaction medium basic. The appearance of black precipitates confirmed the formation of CuS. As post-treatment, the CuS precipitates were collected, washed, ultrasonicated with ethanol, dried at 70 °C overnight, and finally annealed at 150 °C for 2–3 h to improve crystallinity.

2.3 Synthesis of nanohybrid

We prepared a 1 g L^{-1} CNT suspension and added 10 mL to 90 mL of water containing 80 mg of copper sulfide. After two hours of sonification, the mixture was dried at 100 °C to get the solid CuS–CNTs composite. Finally, the CuS NPs and CuS–CNTs nanohybrid were subjected to characterization and application study.

2.4 Photocatalytic experiment

MB dye powder was dissolved in distilled water under magnetic stirring to make a 15 ppm solution. 15 mg of each catalyst (CuS and CuS–CNTs catalyst) was added separately to the (15 ppm) MB dye solution. Then, catalyst-dye solutions were stirred for 30 min in the dark to achieve the equilibrium between adsorption and desorption. A spectrophotometer assessed the quantity of adsorbed MB dye by decreasing the absorption peak (λ_{max} at 666 nm) until a steady value was attained. MB dye photodegradation under visible light (400 watt tungsten lamp) was tested for 100 and 90 min using CuS and CuS–CNTs catalysts. A sample was taken from the catalyst-dye mixture every 10 min and evaluated for absorbance following centrifugal removal of the catalyst. The Beer–Lambert equation was used to assess dye concentration reduction. Finally, the controlled experiments were performed without the catalyst under identical dark and light conditions to assess the catalyst's efficacy in dye degradation by comparing the findings. The degrading efficiency (%) was estimated using the following formula.[23]

$$\%\ \text{Photodegradation} = \frac{C_\text{i} - C_t}{C_\text{i}} \times 100$$

In the above equation, C_i is the original dye concentration, and C_t is the concentration measured at a time 't'.

3. Results and discussion

3.1 Structure elucidation

The crystal phase, grain size, purity, and crystallinity level of a material can be determined through the use of X-ray diffraction. Fig. 1a presents the XRD profiles of bare copper sulfide and the nanohybrid samples. In the XRD spectrum of bare CuS, nine diffraction peaks were observed at the Bragg's angle (2θ) of 27.60°, 29.44°, 31.90°, 32°, 48°, 52.9°, 59.20°, 70.04°, and 73.99°, and 75.47°, corresponding to the (101), (102), (103), (006), (110), (114), (116), (213), and (208) hexagonal crystal planes. These peaks confirmed the successful formation of CuS NPs in a crystalline hexagonal structure. All these observed diffraction peaks are in excellent agreement with JCPDS # 01-1281.[24] The synthesized CuS exhibits high crystallinity and phase purity, as evidenced by sharp characteristic peaks and the absence of any additional signals. In contrast, the XRD pattern of the CuS–CNTs nanohybrid revealed all the peaks of CuS hexagonal phase, as well as an additional hump at $2\theta = 24.7$. The presence of a hump is due to the successful attachment of CNTs to CuS NPs during the synthesis of the CuS–CNTs nanohybrid material. The preservation of all distinctive peaks and the absence of a surplus peak suggest that the addition of CNTs did not affect the crystallographic phase of CuS NPs. Composite-induced strain distorts the crystal lattice and may cause less intense and broader XRD peaks in CuS–CNTs nanohybrid samples than in pristine CuS. This lower intensity could be due to the fact that the CNTs are spread out and absorb X-rays, hiding some pure CuS or a lower CuS–CNTs loading. The grain size was quantified using Scherrer's formula:[25,26]

$$D = \frac{0.94\lambda}{\beta \cos \theta}$$

where 'θ'' stands for the diffraction angle, 'λ' for the X-ray wavelength, and 'β' for the full width at half maximum. The CuS sample's average grain size was found to be 17.4 nm. The small CuS crystallite size and CNTs create a synergistic effect, improving light absorption, charge separation, and overall photocatalytic efficiency of the newly developed nanohybrid.

The FTIR profiles of bare CuS and CuS–CNTs nanohybrid materials were recorded from 4000 to 500 cm^{-1} to identify functional groups and characterize the chemical bonds, as seen in Fig. 1b. A strong and broad band between 3140 cm^{-1} and 3500 cm^{-1} (caused by O–H stretching vibrations) and a sharp band near 1641 cm^{-1} (as a consequence of O–H bending vibrations) confirmed the existence of adsorbed water from the environment.[27,28] The coupling of C=O stretching vibrations is responsible for a weak band near 2289 cm^{-1}, confirming adsorbed CO_2.[29,30] The strong absorption band at 629 cm^{-1}, responsible for Cu–S stretching vibrations, is the most noticeable characteristic confirming the formation of CuS.[31] The bands at 950 cm^{-1} and 1292 cm^{-1} indicate C–O stretching vibrations, representing oxygenated functional groups and C–H stretching vibrations at 2965 cm^{-1} are linked to alkyl groups from organic contaminants, respectively.[32] The CuS–CNTs profile, on the other hand, shows an additional band at 1563 cm^{-1} for graphitic C=C stretching (sp^2 carbon, associated with CNTs).[33]

3.2 Morphological and compositional analysis

The electron micrographs of prepared CuS and CuS–CNTs samples were analyzed for the morphological characteristics, surface texture, dimensions of particles, and distribution pattern. Fig. 2a and b presents the SEM images for bare CuS and CuS–CNTs samples, obtained at different magnifications. Most CuS particles are polyhedral and spherical, ranging from 47 to

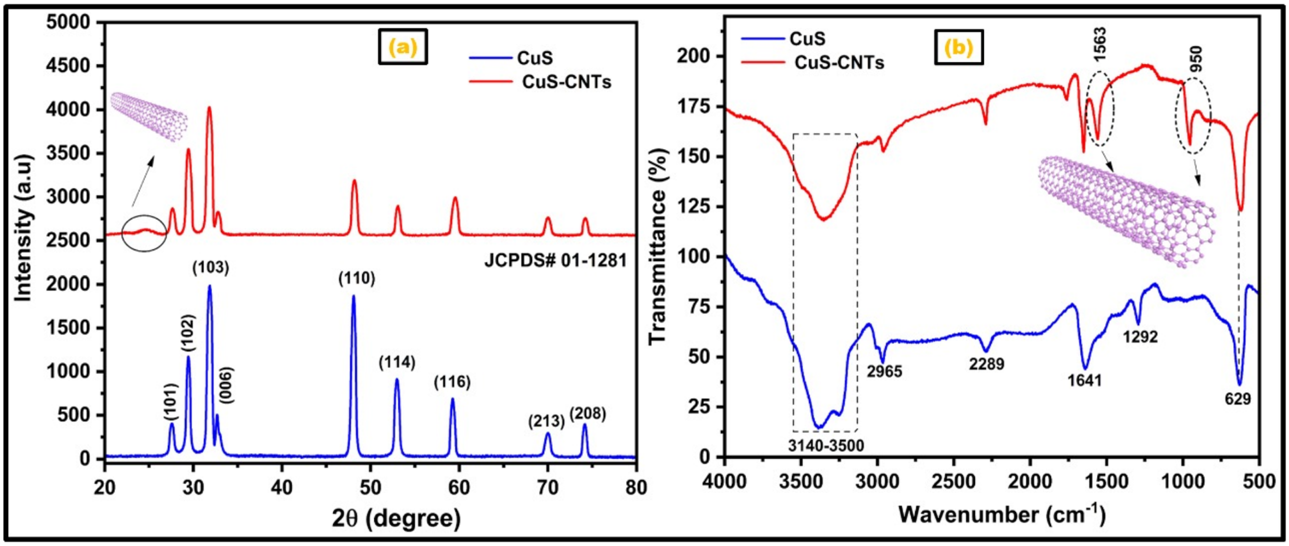

Fig. 1 (a) X-ray diffraction (a) and (b) Infrared spectra of copper sulfide and its CNTs supported nanohybrid.

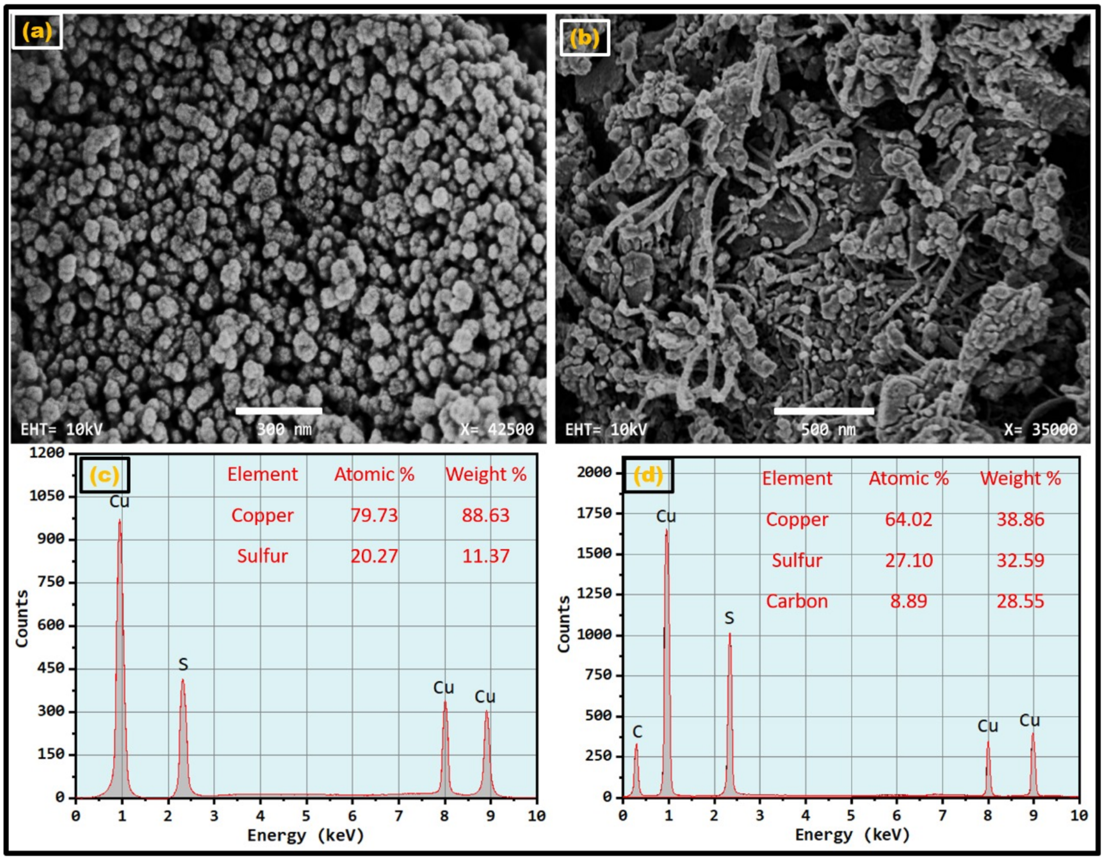

Fig. 2 SEM of (a) copper sulfide and (b) its CNTs-supported nanohybrid; EDX of (c) copper sulfide and (d) its CNTs-supported nanohybrid.

81 nm. Nonetheless, certain particles experience aggregation, resulting in the creation of more prominent clusters. This aggregation adversely affects the surface area of the photocatalyst, thereby diminishing its catalytic efficacy.

In comparison, the SEM image of the CuS–CNTs composite exhibited a hybrid structure whereby CuS nanoparticles (NPs) are evenly scattered throughout the surface of the carbon nanotubes (CNTs). CuS NPs are attached to a fibrous, network-like CNT framework. This structural configuration reduces the CuS particle aggregation rather successfully. The enhanced distribution and reduced aggregation of CuS NPs in the CuS–CNTs composite enhanced the photocatalytic efficacy. Additionally, the synergistic effect of CuS and CNTs leads to better charge separation and transfer, which makes CuS–CNTs potentially useful as photocatalysts for the remediation of the environment.

The EDX analysis of CuS and CuS–CNTs was conducted to ascertain the composition and purity of both synthesized materials. Fig. 2c and d presents the EDX spectra of CuS and CuS–CNTs nanohybrid, covering an energy range from 0 to 10 keV. The EDX spectrum of CuS exhibits four peaks; out of these, three peaks at 0.9 keV, 8 keV, and 8.9 keV denote the existence of Cu, while the third peak at 2.4 keV confirms the attendance of S.[34,35] The absence of any supplementary peak proves the exceptional purity of CuS. In contrast, the EDX spectrum of CuS–CNTs displayed five peaks; out of these, four peaks were identical to the peaks that appeared in the EDX of CuS, while the fifth peak at 0.27 keV confirms the presence of the carbonaceous matrix (CNTs) in the nanohybrid samples.

3.3 Optical and optoelectronic investigations

UV/visible spectroscopy was applied to evaluate the optical behavior of CuS and CuS–CNTs nanocatalysts and to ascertain the band gap energy of CuS. Fig. 3a shows the absorption spectra of both the prepared nanocatalysts (200–800 nm). The absorption spectra of the synthesized nanocatalysts exhibit absorption in both the ultraviolet (UV) and visible regions of light. The absorption edge of CuS–CNTs, extends to 530 nm, exhibiting a red shift and enhanced absorption intensity relative to the absorption edge of CuS at 450 nm.[36] The improved absorption of visible light in CuS–CNTs composites was ascribed to the light-harvesting properties of CNTs.[37] According to the UV/visible study results, the CuS–CNTs nanocatalyst has the potential to perform better as a photocatalyst by utilizing a maximum of light energy.[38] The Tauc's equation was applied to ascertain the band gap energy of CuS nanoparticles.[39,40]

$$(\alpha h\nu)^{1/n} = K(h\nu - E_g)$$

In this equation, the symbol 'K' signifies a constant factor, '$h\nu$' indicates the photon energy, 'E_g' represents the energy band gap, 'α' represents the absorption coefficient, and 'n' is an

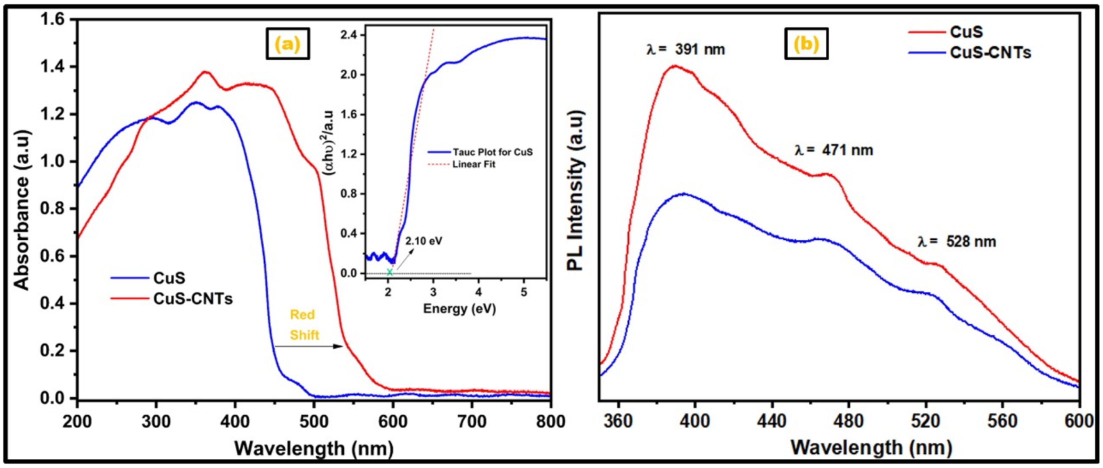

Fig. 3 (a) UV/Vis and (b) PL spectra of copper sulfide and its nanohybrid.

exponential component and is 2 for direct bandgap. A plot of $(\alpha h\nu)^2$ *versus* '*E*' (photon energy) was constructed. The linear section of the curve was subjected to linear fit to compute the band gap of the CuS NPs.[41] Our nanoparticles of CuS demonstrate an optical band gap of 2.10 eV, which is consistent with the reported values (1.6–3.2 eV) for CuS-based nanomaterials.[42–44] This band gap is essential for the effective absorption of visible light, which is essential for the enhancement of photocatalytic activity. The integration of CNTs further improves photoconversion efficiency by reducing charge recombination and broadening light absorption through synergistic interactions, thereby enhancing charge transfer. These benefits underscore the importance of CNTs in the optimization of CuS-based nanocomposites for applications that are driven by visible light.

Photoluminescence (PL) investigates the recombination rate and lifespan of generated charge carriers, with the PL spectrum intensity directly reflecting the electron–hole recombination rate and their brief lifespan. Fig. 3b depicts the PL spectra of CuS and CuS–CNTs in the wavelength range of 300 to 750 nm. The PL spectrum of the CuS sample has high intensity, representing the high recombination rate and shorter life span of charge carriers.[45]

On the other hand, the lower PL intensity for the CuS–CNTs sample exhibits the retarded electron–hole pair recombination and longer lifespan of charge carriers. CNTs in the CuS–CNTs composite are responsible for the reduced PL intensity. Because of their high conductivity and work function relative to CuS, CNTs operate as an electron sink and form a Schottky junction at the CuS interface, allowing electrons to flow from the CuS conduction band to CNTs while leaving holes in the CuS valence band.[46] According to the PL study, the CuS–CNTs composite should perform better photocatalytically than CuS NPs because of its reduced electron–hole recombination rate.

3.4. *I–V* analysis

Pure CuS and CuS–CNTs nanohybrids were tested for electrical conductivity using current–voltage (*I–V*) measurements. This investigation examined how the CNT matrix affected the electrical characteristics of CuS. The uniformly sized pellets of CuS and CuS–CNTs were produced with equal weights using a stainless-steel die. The area and diameter of the pellets were measured using a computerized instrument. Fig. 4a and b depicts the *I–V* profiles for both synthesized nanocatalysts within a voltage range of −10 to 10 V. The *I–V* profile of the pristine CuS sample exhibits non-linearity (semiconductive behavior), characterized by a reduced slope, signifying less electrical conductivity.[47] Conversely, the CuS–CNTs sample demonstrates a nearly linear *I–V* curve (indicative of conductive behavior) with a more pronounced slope, indicating enhanced conductivity.[48] The electrical conductivity derived from the slope was found to be 6.14×10^{-3} Siemens for pristine CuS and 1.365×10^{-2} Siemens for the CuS–CNTs nanohybrid. The improved electrical conductivity of the CuS–CNTs nanohybrid enabled it to boost the kinetics of the photocatalytic process.

3.5 Thermogravimetric analysis

Thermogravimetric analysis (TGA) is a technique employed to assess the thermal robustness of a material, ascertain its moisture level, and measure the carbon content present. Fig. 5 presents the TGA profiles of CuS and CuS–CNTs within the temperature span of 25–900 °C, with a heating rate of 10 °C min^{-1}. The TGA profile for CuS shows a little drop above 100 °C, indicating a weight loss of around 0.7% due to the removal of surface-adsorbed moisture.[49]

No further weight loss up to a temperature of 900 °C indicates the thermal stability of prepared CuS. On the other hand, the CuS–CNTs composite exhibits a 1.4% weight loss around 100 °C due to the removal of physically adsorbed water. The second weight loss, around 12% around 400 °C, is caused by burning carbon-based components (CNTs) in the nanocomposite material, revealing its CNTs content.[50,51] The CuS–CNTs nanohybrid's greater surface area, high porosity, and superior adsorption capacity are evident from its weight loss compared to bare CuS. Furthermore, its stability under high

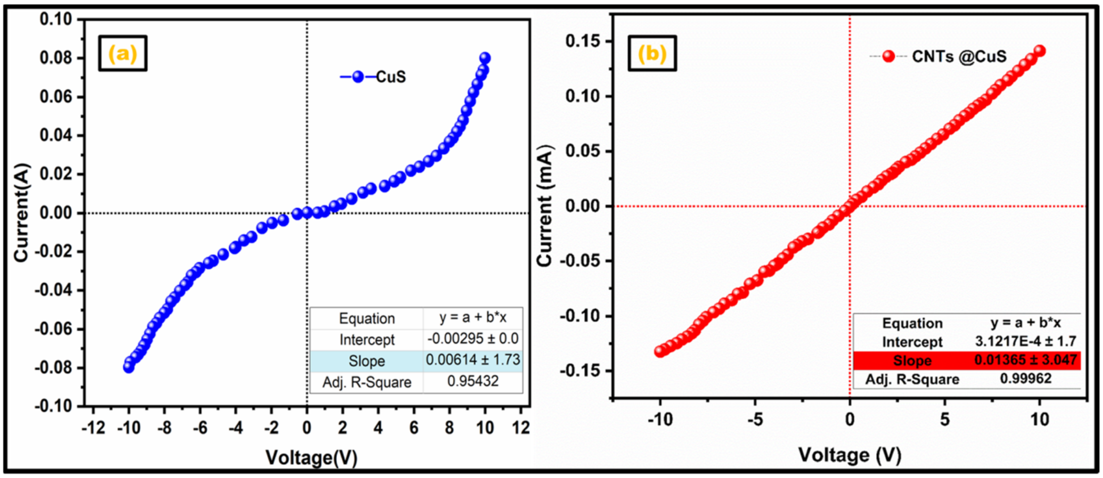

Fig. 4 *I*–*V* plot for (a) copper sulfide and (b) its nanohybrid.

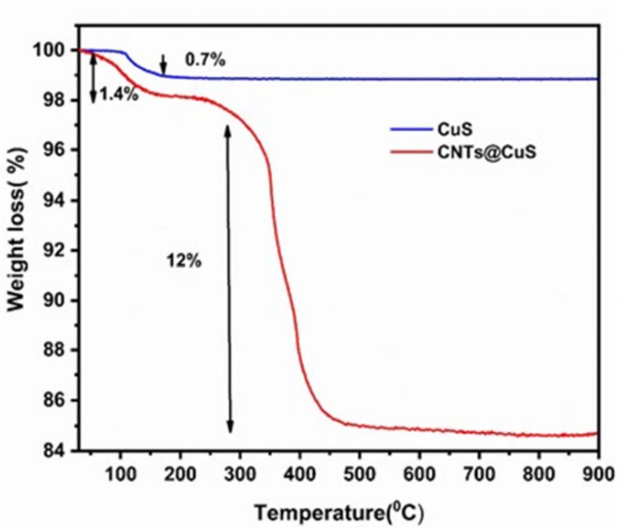

Fig. 5 TGA of copper sulfide and its nanohybrid.

thermal conditions highlights its suitability as a photocatalyst for demanding applications and prolonged operational use.

3.6 Photocatalytic study

The catalytic performance of as-synthesized bare CuS and CuS–CNTs nanocatalysts was examined and compared by executing the MB dye degradation under visible light illumination. The complete elimination of MB dye transpires *via* three separate mechanisms: the physical adsorption of the dye onto the catalyst surface, the photochemical degradation of the dye, and the photolysis of the dye upon being exposed to visible light. A 15 ppm aqueous solution of MB dye was prepared, and its UV/visible absorption spectrum baseline was recorded. The solution was mixed separately with CuS and CuS–CNTs catalysts in dark for 30 min with continual stirring. Subsequently, the visible spectra of both mixtures were recorded to evaluate the adsorption-mediated removal of MB dye.[52] As demonstrated in Fig. 6a, the CuS catalyst absorbed 6.5%, whereas the CuS–CNTs catalyst adsorbed 10.48% of the MB dye during the dark phase. The large surface area-to-volume ratio of CNTs and π–π conjugation between the dye molecules and CNTs are responsible for the superior dye adsorption ability of the CuS–CNTs catalyst.[53] In the second phase, the CuS-dye mixture was irradiated in visible light for 100 min while the CuS–CNTs catalyst was illuminated in visible light for 90 min. The amount of dye photo-chemically degraded was evaluated by recording absorption spectra (400–800 nm) every 10 min, as illustrated in Fig. 6b and c. The concentration of MB dye lowers consistently throughout irradiation, first quicker but slowing down. The CuS catalyst eliminated 65.9% of the MB dye, including 6.5% by adsorption and 59.4% through photochemical processes. Conversely, the CuS–CNTs catalyst removed 100% of MB dye, with 10.48% attributed to physical adsorption and 89.52% due to photodegradation, as seen in Fig. 6d. The synergistic interaction between CuS and CNTs is responsible for the rapid and enhanced catalytic activity of CuS–CNTs in comparison to CuS.

Additionally, establishing a Schottky barrier at their contact allows unidirectional electron transport from the conduction band of CuS to CNTs, decreasing electron–hole recombination.[54] Then, a 15 ppm dye solution was photolyzed without a catalyst under visible light for 100 min to measure dye removal. After 100 min of light exposure, the absorption spectra showed a 2.8% drop in dye concentration, demonstrating that the dye is nearly photolytically stable (Fig. 6d).

We used multiple kinetic models to analyze the experimental data and found that the pseudo-first-order photodegradation model (Adj-*R*-Square > 0.97) was well-suited.

$$-\ln(C_t/C_o) = kt$$

Thus, we linearly fitted the $-\ln C_t/C_o$ *vs.* time (min) plot to get the slopes (rate constant values) for CuS and CuS–CNTs catalysts, as illustrated in Fig. 7a. The MB dye degradation rate constants for CuS and CuS–CNTs catalysts were determined to

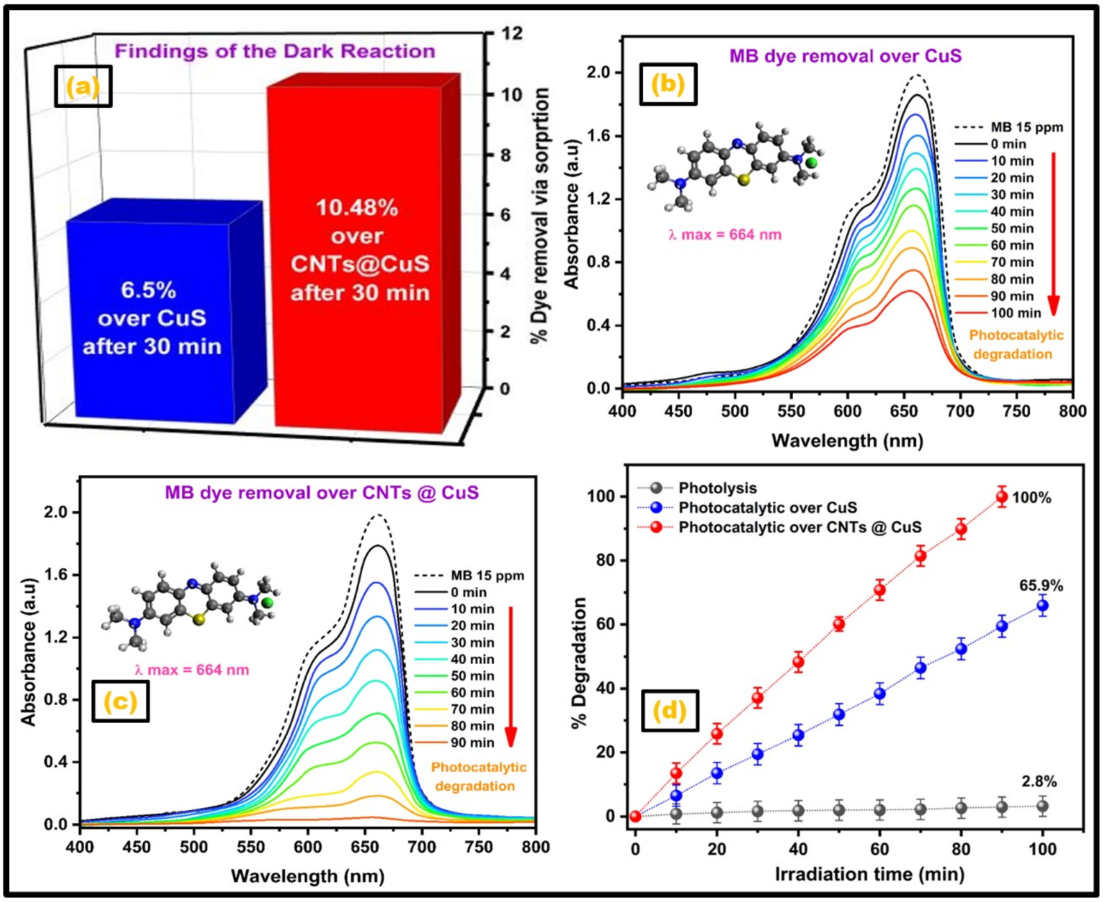

Fig. 6 (a) Dye adsorption study, time-dependent MB dye degradation over (b) copper sulfide and (c) its nanohybrid, and (d) MB dye degradation % *via* photocatalysis and photolysis.

be 0.01048 $\min^{-1}$ and 0.02443 $\min^{-1}$, respectively, with CuS–CNTs having a rate constant 2.33 times larger than CuS. The CNTs in CuS NPs are fully credited for the CuS–CNTs catalyst's higher rate constant value, as they facilitate faster electron transit and reduce charge recombination.

Essential characteristics of an effective catalyst are high photocatalytic efficiency, strong photostability, and good reproducibility, as these properties cut costs and minimize environmental concerns. The reusability and photostability of the CuS–CNTs nanocatalyst were examined by degrading MB dye under visible light in five cycles, each lasting 100 min. At the end of each cycle, the catalyst was retrieved by centrifugation, rinsed, dried, and reused with a fresh dye solution of the same concentration. Fig. 7b depicts the degradation of MB dye by graphing the concentration ratio (C_t/C_o) on the y-axis against the elapsed time on the x-axis for all five cycles. The degrading efficiency stayed almost the same over cycles, dropping only 2.15% from the first to the fifth. This small decrease in degradation efficiency may be due to byproducts blocking catalyst active sites or catalyst loss during washing and drying.[55,56] No noticeable drop in the catalytic activity of the catalyst after five cycles of reuse indicated that the catalyst retaining high catalytic efficiency exhibits good reproducibility and photostability.[57]

Scavenging tests were conducted using *tert*-butyl alcohol (TBA), ethylenediaminetetraacetic acid (EDTA), and benzoquinone (BQ) as effective scavengers for hydroxyl radicals ($^{\bullet}$OH), holes (h^+), and superoxide radicals ($O_2^{\bullet-}$), respectively. As shown in Fig. 8a, the rate constant decreased from 0.024 $\min^{-1}$ to 0.018 $\min^{-1}$, 0.013 $\min^{-1}$, and 0.003 $\min^{-1}$ in the presence of BQ, EDTA, and TBA, respectively. The significant decline observed in the presence of TBA suggests that hydroxyl radicals ($^{\bullet}$OH) play a predominant role in the degradation of methylene blue (MB) dye during the CuS–CNTs-driven photocatalytic process.

The potential values of the valence band (E_{VB}) and conduction band (E_{CB}), along with the band gap energy, are crucial for comprehending the degradation mechanism of MB dye by the CuS–CNTs catalyst under visible light.[58] Consequently, E_{VB} and E_{CB} values were calculated using eqn (1) and (2) to understand better the charge separation, charge transfer routes, and redox reactions involved in catalytic activity.[59,60]

$$E_{CB} = \chi - E_e - 0.5\ E_g \tag{1}$$

$$E_{VB} = E_g + E_{CB} \tag{2}$$

In these equations, E_e is the energy of free electrons, E_g is the band gap energy, and χ stands for absolute electronegativity.

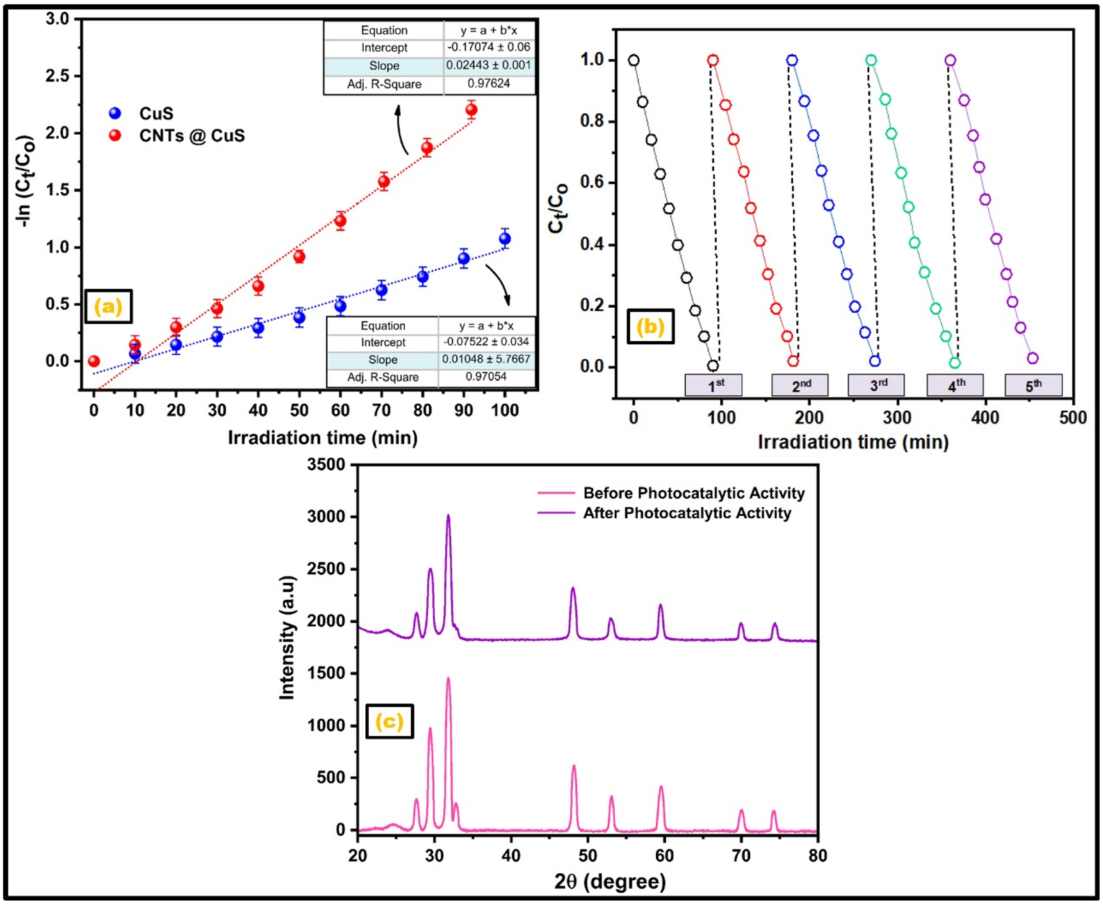

Fig. 7 (a) Kinetics study (b) reusability of nanohybrid and (c) XRD pattern post reusability test.

The E_{VB} and E_{CB} of the prepared CuS–CNTs photocatalyst were 1.83 eV and −0.27 eV, respectively, with a band gap of 2.10 eV. Fig. 8b depicts the MB dye degradation route utilizing CuS–CNTs as a catalyst under visible light. The CuS–CNT catalyst absorbs visible light photons (with energy ≥2.1 eV) when exposed to visible light, causing electron transition from the valence to the conduction band.[61] Consequently, positive holes are produced in the valence band, and photogenerated electrons in the conduction band.[62] The conduction band electrons (e^-) in CuS are transferred to the CNTs, which act as electron acceptors and transporters. This electron migration enhances charge separation, thereby increasing the availability of electrons for reduction reactions.

Evidently, CuS alone cannot reduce the molecular oxygen to superoxide free radical, hence, CNTs may facilitate electron transfer to molecular oxygen to generate superoxide free radicals.[63] The electrons in the conduction band and at the CNTs, have sufficient potential to allowing a two-electron reduction pathway, leading to H_2O_2 formation. Formed H_2O_2 generate $OH^{\bullet}$ either by photolytic decomposition or electron induced breakdown. Scavenging tests findings reveal the role of superoxide radical as well, hence there is possibility that H_2O_2 undergoes hole induced oxidation to form hydroperoxyl radical ($^{\bullet}HO_2$). The electrons from the conduction band of the CuS or from the CNTs reduce the hydroperoxyl radical into superoxide free radical. Highly reactive hydroxide radicals ($OH^{\bullet}$) and superoxide radicals ($O_2^{\bullet -}$), produced from oxidation and reduction processes, respectively, engage in redox reactions with MB dye, resulting in its decomposition into smaller, simple, and harmless molecules such as H_2O, CO_2, *etc.*

The following equations depict the whole reaction mechanism.

$$\mathrm{CuS} + h\nu \rightarrow \mathrm{CuS}\,[\mathrm{e}^-{}_{(\mathrm{CB})} + \mathrm{h}^+{}_{(\mathrm{VB})}]$$

$$\mathrm{CuS}\,[\mathrm{e}^-{}_{(\mathrm{CB})}] + \mathrm{CNTs} \rightarrow \mathrm{CNTs}\,(\mathrm{e}^-)$$

$$\mathrm{O_2} + 2\mathrm{H}^+ + 2\mathrm{e}^- \rightarrow \mathrm{H_2O_2}$$

$$\mathrm{H_2O_2} + h\nu \rightarrow 2\mathrm{OH}^{\bullet}$$

$$\mathrm{H_2O_2} + \mathrm{e}^- \rightarrow \mathrm{OH}^{\bullet} + \mathrm{OH}^-$$

$$\mathrm{H_2O_2} + \mathrm{h}^+ \rightarrow \mathrm{HO}_2^{\bullet} + \mathrm{H}^+$$

$$\mathrm{HO}_2^{\bullet} + \mathrm{e}^- \rightarrow \mathrm{O}_2^{\bullet -} + \mathrm{H}^+$$

$$\mathrm{OH}^{\bullet} + \mathrm{O}_2^{\bullet -} + \mathrm{MB\ dye} \rightarrow \text{non-toxic degradation products}$$

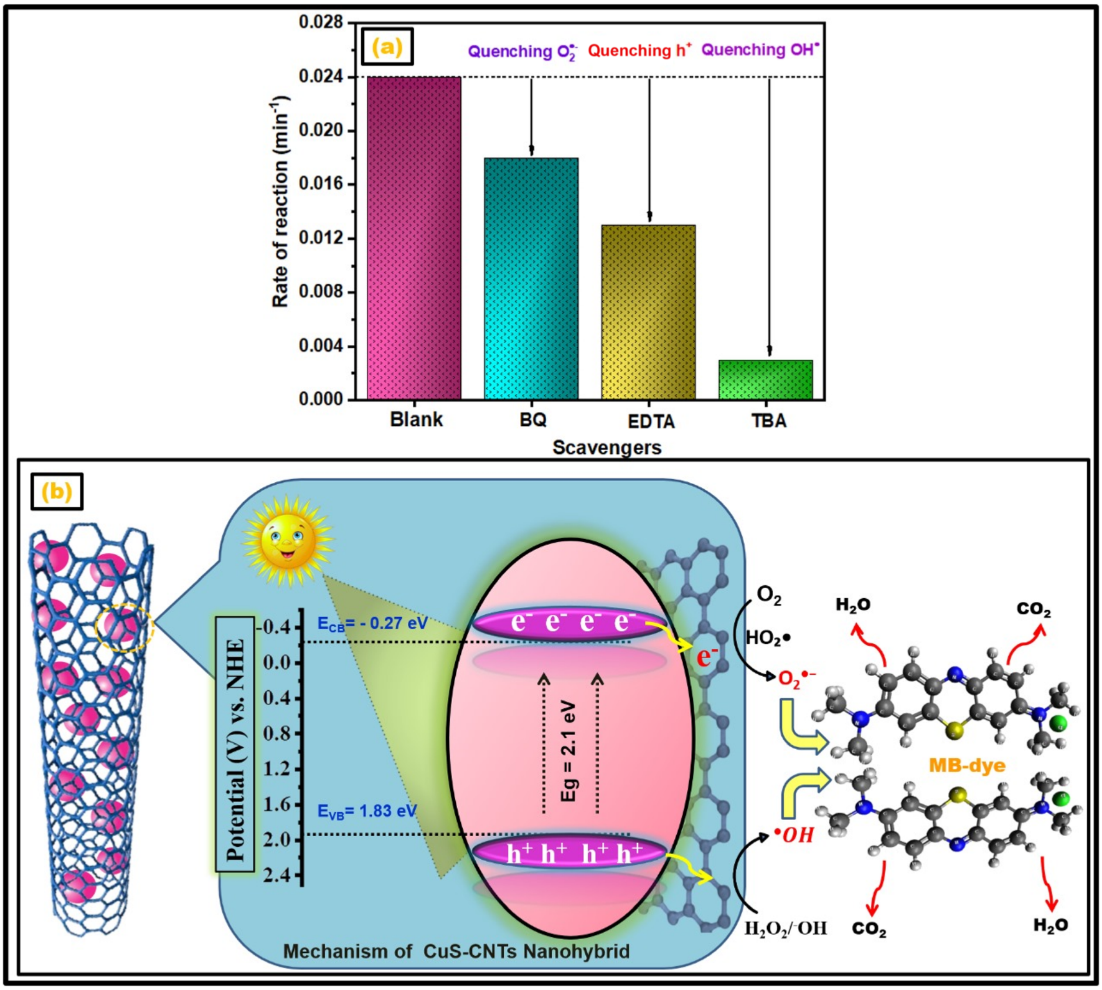

Fig. 8 (a) Results of the quenching tests and (b) proposed mechanism based on the quenching tests, illustrating the degradation of methylene blue (MB) dye over the CuS–CNTs nanohybrid.

4. Conclusions

In this study, CuS nanoparticles and CuS–CNT nanohybrids were synthesized *via* an ultrasonication-assisted co-precipitation approach and evaluated as photocatalysts for wastewater treatment. Structural and morphological analyses confirmed strong interactions between CuS and CNTs, enhancing photocatalytic performance. The CuS–CNT nanohybrid achieved nearly 100% MB dye degradation in 90 min under visible light, whereas pristine CuS reached only 65.9% after 100 min. This improvement is attributed to stronger visible-light absorption, increased electron–hole generation, and reduced recombination rates as verified by UV-Vis and PL analyses. CNTs further facilitated charge transfer due to their high electrical conductivity. The uniform CuS distribution on CNTs minimized aggregation, increased surface area, and improved dye adsorption (10.48% for CuS–CNTs *vs.* 6.5% for CuS). Moreover, the catalyst retained 97.85% of its efficiency after five cycles, demonstrating excellent stability. These results highlight the potential of CuS–CNT nanohybrids for wastewater treatment. Future work should explore their performance in real wastewater, optimize composition and conditions, and assess scalability for industrial applications.

Data availability

Data will be available upon request.

Conflicts of interest

The authors declare that they have no known competing financial interests or personal relationships that could have appeared to influence the work reported in this paper.

Acknowledgements/Funding

This work was supported and funded by the Deanship of Scientific Research at Imam Mohammad Ibn Saud Islamic University (IMSIU) (grant number IMSIU-DDRSP2502).

References

1 V. K. Gaur, P. Sharma, R. Sirohi, M. K. Awasthi, C.-G. Dussap and A. Pandey, *J. Hazard Mater.*, 2020, **398**, 123019.

2 Q. Zhang, W. Li, J. Peng, L. Xue and G. He, *Green Chem.*, 2024, **26**, 7091–7100.

3 T. Islam, M. R. Repon, T. Islam, Z. Sarwar and M. M. Rahman, *Environ. Sci. Pollut. Res.*, 2023, **30**, 9207–9242.

4 X. Yan, J. Feng, P. Li, J. Li, B. Ren, S. Gao and R. Cao, *Inorg. Chem. Commun.*, 2021, **131**, 108796.

5 Q.-Q. Zhang, G.-G. Ying, C.-G. Pan, Y.-S. Liu and J.-L. Zhao, *Environ. Sci. Technol.*, 2015, **49**, 6772–6782.

6 G. Wang and A. Fakhri, *Int. J. Biol. Macromol.*, 2020, **155**, 36–41.

7 H. M. Munjur, M. N. Hasan, M. R. Awual, M. M. Islam, M. Shenashen and J. Iqbal, *J. Mol. Liq.*, 2020, **319**, 114356.

8 Z. Heidari, R. Alizadeh, A. Ebadi, N. Oturan and M. A. Oturan, *Sep. Purif. Technol.*, 2020, **242**, 116800.

9 A. Irshad, F. Farooq, M. F. Warsi, N. Shaheen, A. Y. Elnaggar, E. E. Hussein, Z. M. El-Bahy and M. Shahid, *FlatChem*, 2022, **31**, 100325.

10 Z. Ali, M. Aadil, B. zainab, M. H. Rasool, W. Hassan, S. Mubarik, Z. Ahmad, N. A. Almuhous, A. A. Alothman and M. Hussain, *Inorg. Chem. Commun.*, 2023, **157**, 111399.

11 W. Qu, D. He, H. Huang, Y. Guo, Y. Tang and R.-J. Song, *J. Mater. Sci.*, 2020, **55**, 7268–7282.

12 Y. Feng, X. Su, Y. Chen, Y. Liu, X. Zhao, C. Lu, Y. Ma, G. Lu and M. Ma, *Mater. Res. Bull.*, 2023, **162**, 112207.

13 H. Kumari, S. M. Ibrahim, A. A. Tahir, R. Ranga, S. Chahal, S. Devi, S. Sharma, S. Kumar, P. Kumar and S. Kumar, *Water, Air, Soil Pollut.*, 2023, **234**, 349.

14 A. Anum, S. M. Ibrahim, A. A. Tahir, M. A. Nazir, M. Malik, S. S. A. Shah, A. Ehsan, M. A. Wattoo and A. ur Rehman, *Inorg. Chem. Commun.*, 2023, **157**, 111268.

15 L. Wang, L. Liu, Y. Li, Y. Xu, W. Nie, Z. Cheng, Q. Zhou, L. Wang and Z. Fan, *Adv. Energy Mater.*, 2024, **14**, 2303346.

16 K. El Akeb, H. Bessaha, H. Aguedal, M. Bouraada, B. Azambre and M. E. A. E. Elmeliani, *J. Water Proc. Eng.*, 2024, **65**, 105866.

17 B. Kaushik, S. Yadav, P. Rana, K. Solanki, D. Rawat and R. Sharma, *Appl. Surf. Sci.*, 2022, **590**, 153053.

18 X.-L. Luo, Y.-X. Yang, Z.-L. Wang, S.-Y. Yang and Y.-H. Xu, *Mater. Res. Bull.*, 2022, **156**, 111985.

19 K. K. Mandari, N. Son and M. Kang, *J. Colloid Interface Sci.*, 2022, **615**, 740–751.

20 R. Wang, G. Shan, T. Wang, D. Yin and Y. Chen, *J. Alloys Compd.*, 2021, **864**, 158591.

21 J. Zhang, M. Dai, S. Zhang, M. Dai, P. Zhang, S. Wang and Z. He, *Sol. RRL*, 2022, **6**, 2200243.

22 A. Yasmeen, A. M. Afzal, M. W. Iqbal, S. Mumtaz, M. Ouladsmane, M. Usman and S. M. Wabaidur, *Appl. Nanosci.*, 2023, **13**, 6471–6487.

23 J. Yadav and O. Sahu, *Ceram. Int.*, 2023, **49**, 24831–24851.

24 M. Khan, M. I. Abdullah, A. Samad, Z. Shao, T. Mushiana, A. Akhtar, A. Hameed, N. Zhang, U. Schwingenschlögl and M. Ma, *Small*, 2023, **19**, 2205499.

25 R. Mandal, S. Pramanik, P. K. Kuiri, B. Mukherjee and R. Nath, *Opt. Mater.*, 2024, **155**, 115917.

26 F. Alresheedi, *J. Mater. Res. Technol.*, 2021, **12**, 2104–2113.

27 S. Mandal, C. Hazra, S. Jena, P. Kumar, R. Sen, S. Das and K. Das, *J. Ind. Eng. Chem.*, 2024, **129**, 352–364.

28 M. Hussain, M. Aadil, E. W. Cochran, S. Zulfiqar, W. Hassan, T. Kousar, H. H. Somaily and F. Mahmood, *Inorg. Chem. Commun.*, 2024, **160**, 112010.

29 J. Liu, B. Li, V. Martins, Y. Huang and Y. Song, *J. Phys. Chem. C.*, 2024, **128**, 8007–8015.

30 M. Rao, H. Xia, Y. Xu, G. Jiang, Q. Zhang, Y. Yuan and L. Zhang, *Hydrometallurgy*, 2024, **230**, 106385.

31 X. Liu, T. Liu, Y. Zhou, J. Wen, J. Dong, C. Chang and W. Zheng, *J. Phys. Chem. Solids*, 2024, **185**, 111781.

32 Y. Ren and Z. Zhang, *Sep. Sci. Technol.*, 2024, **59**, 1799–1810.

33 M. Fang, R. He, J. Zhou, H. Fei and K. Yang, *J. Energy Storage*, 2024, **86**, 111244.

34 M. Shahrashoub and S. Bakhtiari, *Microporous Mesoporous Mater.*, 2021, **311**, 110692.

35 B. Qasim, K. Jabbour, M. Ouladsmane, M. S. Waheed, M. Abdullah, N. Bano, S. Manzoor, M. Sillanpää and M. N. Ashiq, *J. Mater. Sci.: Mater. Electron.*, 2024, **35**, 445.

36 M. Das, D. Das, S. Sil and P. P. Ray, *Nanoscale Adv.*, 2023, **5**, 3655–3663.

37 G. Liu, M. Liao, Z. Zhang, H. Wang, D. Chen and Y. Feng, *Sep. Purif. Technol.*, 2020, **244**, 116618.

38 J. P. Jeon, D. H. Kweon, B. J. Jang, M. J. Ju and J. B. Baek, *Adv. Sustainable Syst.*, 2020, **4**, 2000197.

39 M. s. Rohokale, D. Dhabliya, T. Sathish, V. Vijayan and N. Senthilkumar, *Phys. B*, 2021, **610**, 412902.

40 B. Al Alwan, M. Aadil, A. Khalid, A. Alazmi, A. El Jery, M. R. Alrahili, M. M. Hossin, M. I. Saleem and M. El-Khatib, *Ceram. Int.*, 2024, **50**, 52583–52594.

41 N. ul Ain, A. Aamir, Y. Khan, M.-u. Rehman and D.-J. Lin, *Mater. Chem. Phys.*, 2020, **242**, 122408.

42 R. S. Christy and J. T. Kumaran, *J. Non-Oxide Glasses.*, 2014, **6**, 13–22.

43 S. C. K, K. Jagadish, H. Bhatt, Y. Jadhav and S. R. Rondiya, *J. Phys. Chem. C.*, 2024, **128**, 20205–20214.

44 K. R. Nemade and S. A. Waghuley, *Mater. Sci. Semicond. Process.*, 2015, **39**, 781–785.

45 M. Siddiq, A. G. Taki, M. Aadil, S. Mubarik, E. W. Cochran, S. Zulfiqar, A. A. Mohammed and S. Ijaz, *Ceram. Int.*, 2023, **49**, 36590–36599.

46 I. Ahmad, S. Shukrullah, M. Y. Naz, E. Ahmed and M. Ahmad, *Int. J. Hydrogen Energy*, 2022, **47**, 9283–9294.

47 H. Sabeeh, M. Aadil, S. Zulfiqar, A. Rasheed, N. F. Al-Khalli, P. O. Agboola, S. Haider, M. F. Warsi and I. Shakir, *Ceram. Int.*, 2021, **47**, 13613–13621.

48 P. O. Agboola, S. Haider and I. Shakir, *Ceram. Int.*, 2022, **48**, 10136–10143.

49 P. Akbarzadeh and N. Koukabi, *Res. Chem. Intermed.*, 2020, **46**, 4955–4969.

50 N. Chandel, M. Kapurderiya, A. Kanse, R. Rohini and T. Sreekumar, *Polym. Compos.*, 2023, **44**, 8589–8600.

51 M. Aldrdery, M. Aadil, A. Khalid, M. R. Alrahili, M. Elhadi, F. Alresheedi, M. Algarni, M. R. El-Aassar and A. E. Jery, *Surf. Interfaces*, 2024, **55**, 105396.

52 H. H. Ali, M. R. Karim, B. Al Alwan, H. D. Alkhaldi, A. Khalid, M. R. Alrahili, M. Naeem, M. Aadil and A. El Jery, *Ceram. Int.*, 2024, **50**, 52572–52582.

53 J. Di, S. Li, Z. Zhao, Y. Huang, Y. A. Jia and H. Zheng, *Chem. Eng. J.*, 2015, **281**, 60–68.

54 Z. Chen, Z. Wei, L. Yang, L. Zheng, W. Cao, S. Zhang, J. Zou and S. Luo, *Chem. Eng. J.*, 2023, **475**, 146236.

55 A. Kumar, M. Khan, J. He and I. M. Lo, *Appl. Catal. B Environ.*, 2020, **270**, 118898.

56 L. Xu, S. Z. Zhang, W. Li and Z. H. Zhang, *Chem.–Eur. J.*, 2021, **27**, 5483–5491.

57 T. Ajeesha, A. Ashwini, M. George, A. Manikandan, J. A. Mary, Y. Slimani, M. A. Almessiere and A. Baykal, *Phys. B*, 2021, **606**, 412660.

58 G. Cabello-Guzmán, M. Seguel, L. Fernández, C. Caro, C. Suarez, M. Matus, C. Cifuentes, F. Bustos and K. Ariz, *Inorg. Chem. Commun.*, 2023, **152**, 110695.

59 Y. Lu, R. Jin, Y. Qiao, W. Liu, K. Wang, X. Wang and C. Wang, *Int. J. Electrochem. Sci.*, 2020, **15**, 10243–10252.

60 R. H. Alshammari, M. Aadil, T. Kousar, U. Maqbool, Z. Ahmad, A. M. Alswieleh, T. S. Algarni and M. Naeem, *Opt. Mater.*, 2023, **144**, 114314.

61 M. Ishfaq, W. Hassan, M. Sabir, H. H. Somaily, S. K. Hachim, Z. J. Kadhim, H. A. Lafta, Y. S. Alnassar, A. M. Rheima, S. R. Ejaz and M. Aadil, *Ceram. Int.*, 2022, **48**, 34590–34601.

62 R. Zhong, H. Liao, Q. Deng, X. Zou and L. Wu, *J. Mol. Struct.*, 2022, **1259**, 132768.

63 H. K. Sharma, S. K. Sharma, K. Vemula, A. R. Koirala, H. M. Yadav and B. P. Singh, *Solid State Sci.*, 2021, **112**, 106492.